Revision 1

'Silicified' pyrochlore from nepheline syenite (mariupolite) of the Mariupol Massif, SE Ukraine: a new insight into the role of silicon in the pyrochlore structure

Magdalena Dumańska-Słowik[1], Adam Pieczka[1], Gioacchino Tempesta[2], Zbigniew Olejniczak[3] and Wiesław Heflik[1]

[1] Department of Mineralogy, Petrography and Geochemistry, Faculty of Geology, Geophysics and Environmental Protection, AGH – University of Science and Technology, Kraków 30-059, 30 Mickiewicza Av., Poland, e-mail: dumanska@uci.agh.edu.pl

[2] Dipartimento Geomineralogico, Università degli Studi di Bari, Via Orabona, 4, I-70125, Bari, Italy

[3] Department of Magnetic Resonance Spectroscopy, The Henryk Niewodniczański Institute of Nuclear Physics, Polish Academy of Sciences, 152 Radzikowski Str., 31-342 Kraków, Poland

Abstract

Pyrochlore-supergroup minerals containing relatively high Si concentration are quite common in various geochemical parageneses, e.g., carbonatites, alkaline syenites, pegmatites. However, the role of Si and the mechanism of its incorporation into the structure of these minerals, although widely discussed, have not been explained definitively. Our paper reports the results of comprehensive SEM, EPMA, XRD, TEM and MAS-NMR studies performed for the first time on a natural pyrochlore, which is the late-magmatic to early hydrothermal accessory component of the nepheline syenite in the alkaline Mariupol massif in Ukraine. It represents partly metamict, patchy-zoned, *A*-cation depleted, REE-, U- and Th-bearing

fluornatropyrochlore, locally exceptionally rich in SiO_2 (up to 13.01 wt%) that underwent both primary and secondary alterations, leading to kenopyrochlore or hydropyrochlore species. The primary alteration was induced by high-temperature, Ca^{2+}- and Si^{4+}-rich, and F^- moderate fluids, which affected only some domains of the pyrochlore crystals and resulted in filling the *A* site vacancies mainly by Ca^{2+}, but also Mn^{2+}, Sr^{2+} and K^+. The secondary alteration, induced by the exposure of the host rock to ground water driving fluid-mediated coupled dissolution-reprecipitation process, affected the whole pyrochlore crystals (both Si-enriched and Si-free domains) and caused, among others, the leaching of some *A*- and *Y*-site components. TEM investigations indicate that the selected area electron diffraction patterns taken from Si-poor areas show strong and sharp diffraction spots related to well-crystalline pyrochlore, whereas the Si-rich areas show weaker spots with a diffuse diffraction halo that are typical of metamict material. Due to the fact that no intergrowth with other Si-bearing phases was observed in the TEM images even at very high magnification, it might be concluded that Si^{4+} can occupy severely alpha-decay damaged and chemically altered portions of this structure. The absence of Si in the sixfold-coordinated *B* site has been corroborated both by compositional relationships, and by the lack of any $^{[6]}Si^{4+}$ signal around -200 ppm in the MAS-NMR spectrum. A broad signal in the spectrum appearing at around -84 ppm, points to an amorphous species with tetrahedrally-coordinated Si, close to $Q^{(2)}$ species defined as Si atom with two bridging oxygens, i.e. $[Si(OSi)_2(-)_2]$, in the form of finite-length chain-like structures, located in the damaged *A* and *B* sites of the primary structure.

Keywords: Si-rich pyrochlore, formula, geochemical alteration, metamictization, $Q^{(2)}$ species

Introduction

The pyrochlore-group minerals occur predominantly as accessory components in nepheline syenites, carbonatites and granitic pegmatites, and they are stable under a wide range of P-T

conditions, varying from igneous to near-surface. Many possibilities of the isomorphic replacement at the *A* and *Y* sites are responsible for a wide compositional variation within this group (Atencio et al. 2010). Among many cations that can be incorporated into the pyrochlore structure, the role of Si^{4+} has been debated for a long time. A number of explanations have been proposed to clarify the mechanism of Si incorporation into natural pyrochlores, starting from the presence of Si-bearing impurities (Hogarth 1989), to the possible presence of Si in an amorphous or dispersed state (Voloshin et al. 1989). According to Chakhmouradian and Mitchell (2002), the common, although enigmatic, incorporation of Si in the pyrochlore could be also explained by the submicroscopic intergrowth of pyrochlore with komarovite, $(H,Ca,Na)_2(Nb,Ti)_2Si_2O_{10}(OH,F)_2$, which has a layered structure, consisting of pyrochlore slabs connected by four-membered tetrahedral silicate rings (Krivokoneva et al. 1979; Balić-Žunić et al. 2002; Ferraris et al. 2004). Luca et al. (2005) performed the X-ray powder diffraction and NMR spectroscopic studies of the synthetic Si-doped antimonic acid $Sb_2O_5 \cdot 4H_2O$, exhibiting the pyrochlore-type structure. They suggested that Si^{4+} can be present in the tetrahedral coordination in the form of isolated $Si(OH)_4$ groups located in hexagonal channels around the *A* site, a structural site that commonly is partly vacant even in well-crystallized pyrochlore species. The location of Si substituting for Sb^{5+} at the *B* site in this antimony pyrochlore was considered to be untenable, because the large difference in the ionic radii between $^{VI}Sb^{5+}$ and $^{VI}Si^{4+}$ should cause a significant volume contraction, which was not observed. Bonazzi et al. (2006) proposed an alternative mechanism for the incorporation of Si^{4+} in the pyrochlore structure. On the basis of structure refinement (SREF) and transmission electron microscopy (TEM) studies of the Si-rich pyrochlore from Narssârssuk, Greenland, they inferred that a fraction (~30–50 %) of the Si detected by the electron microprobe analysis (EMPA) occurs in the octahedral *B* site, whereas the remaining 70–50% enters the radiation-damaged, H_2O-rich portions of such, partly altered pyrochlore. On the basis of the latter

observation, Atencio et al. (2010) suggested that a low content of Si that is observed in the electron probe microanalyses could be assigned to the *B*-site population or related to a contaminant phase.

Minerals of the pyrochlore supergroup represent a group of cubic oxides (space group symmetry $Fd\bar{3}m$) with the general formula $A_{2-m}B_2X_{6-w}Y_{1-n}$. The *A* site is typically occupied by large cations such as Na^{+}, Ca^{2+}, Sr^{2+}, Pb^{2+}, Sn^{2+}, Sb^{3+}, Y^{3+}, U^{4+}, sometimes also by Ag^{+}, Mn^{2+}, Ba^{2+}, Fe^{2+}, Bi^{3+}, REE^{3+}, Sc^{3+} and Th^{4+}, by H_2O molecules, or remains unfilled (vacancy). The *B* site contains mainly Nb^{5+}, Ta^{5+}, Ti^{4+}, Sb^{5+} and W^{6+}, subordinate V^{5+}, Sn^{4+}, Zr^{4+}, Hf^{4+}, Fe^{3+}, Mg^{2+}, Al^{3+}, and possibly Si^{4+}. The *X* anion position is mostly occupied by O^{2-}, but it can also include subordinate OH^{-} and F^{-}, whereas *Y* is typically OH^{-}, F^{-} O^{2-}, but can also be vacancy, H_2O, or may contain very large monovalent cations such as K^{+}, Rb^{+}, and Cs^{+} (Atencio et al. 2010). The symbols *m*, *w* and *n* indicate incomplete occupancies of the *A*, *X* and *Y* sites, respectively, with the following ranges: $m = 0.0–2.0$ (Brugger et al. 1997), $w = 0.0–0.7$ and $n = 0.0–1.0$ (Lumpkin and Ewing 1995).

In the classification of the supergroup, following the recommendation of the Commission on New Minerals, Nomenclature and Classification of the International Mineralogical Association (CNMNC-IMA), five major groups are defined on the basis of the *B*-site occupancy by M^{4+}, M^{5+} and M^{6+} cations: (1) **betafite** , when $M^{4+} > M^{5+}$ and M^{6+}, and Ti^{4+} is the dominant M^{4+} cation; (2) **pyrochlore**, when $M^{5+} > M^{4+}$ and M^{6+}, and Nb^{5+} is the dominant M^{5+} cation; (3) **microlite**, when $M^{5+} > M^{4+}$ and M^{6+}, and Ta^{5+} is the dominant M^{5+} cation; (4) **romèite**, when $M^{5+} > M^{4+}$ and M^{6+}, and Sb^{5+} is the dominant M^{5+} cation, and (5) **elsmoreite**, when $M^{6+} > M^{4+}$ and M^{5+}, and W^{6+} is the dominant M^{6+} cation (Atencio et al. 2010).

Due to complex composition of the members of the pyrochlore supergroup, the chemical effects of their alteration are very complicated. Lumpkin and Ewing (1995) discussed the so-called primary, secondary, and transitional alteration of pyrochlores of different origin,

finding columbite, fersmite, lueshite, bästnaesite and several Fe-Ti oxides as the most common products of such alterations. Wall et al. (1996) noted also a reaction rim composed of crandallite around the altered pyrochlore.

Initially, the main objective of this work was to provide a microchemical characterization of pyrochlore-group minerals selected from *mariupolite* (a leucocratic variety of aegirine-albite nepheline syenite) of the eastern Priazovian region, in the north-eastern part of the alkaline Mariupol massif (the Mazurovski Field) in SE Ukraine. However, a relatively high concentration of SiO_2 in the pyrochlore, up to 13.01 wt% in individual spots, made it possible to focus on the Si role in the natural species. To this aim, we applied scanning (SEM) and transmission (TEM) electron microscopy, electron probe microanalyses (EMPA), X-ray powder diffraction (XRD) and Magic-Angle-Spinning Nuclear Magnetic Resonance (MAS-NMR) spectroscopy.

Geological setting and sample description

The alkaline Mariupol massif in the south-eastern Ukraine, covering an area of 34 km^2, is a unique province of alkaline magmatism dating back to the Proterozoic age *ca.* 1.8 Ga (Volkova 2000, Krivdik et al. 2007). Geology and genesis of this massif was discussed in detail by Donskoy (1982), Volkova (2000; 2001) and Krivdik et al. (2007). The core of the massif is generally composed of nepheline-bearing, alkali feldspar syenites (*pulaskites*), with foyaites, syenites, aegirine-albite nepheline syenites (*mariupolites)*, and ultramafic and mafic rocks (peridotites, pyroxenites and gabbros) occurring outwards.

The samples of mariupolite-hosted pyrochlore were collected in the Mazurovski Field, in the north-eastern part of the massif. They represent a leucocratic, fine- to medium-crystalline variety of mariupolite with porphyritic, mainly chaotic and, in places, fluidal texture, composed of plagioclase ($Ab_{94-92}An_{6-8}$) and nepheline as the main components, and

subordinate lepidomelane, pyrochlore, sodalite, natrolite, aegirine, cancrinite, zircon, britholite-(Ce), fluorapatite, monazite and chlorite (Dumańska-Słowik et al., 2011a, 2011b, 2012). Euhedral to occasionally subhedral crystals of pyrochlore (20–100 μm in size) occur in the interstices of albite and some of them have a characteristic reaction rim consisting of the needle-shaped Fe-bearing chlorite. Only a few of them exhibit poor zoning, very often with irregular lighter and darker patchy domains in back-scattered-electron (BSE) images, and numerous microfractures (Fig. 1).

Experimental methods

Back-scattered electron (BSE) images of polished sections were obtained using a FEI Quanta 200 FEG scanning electron microscope equipped with the energy dispersive X-ray spectrometer (EDS) of EDAX. The system operated at 25 kV accelerating voltage in a high-vacuum mode.

Electron probe microanalyses of four crystals of pyrochlore were carried out at the Inter-Institute Analytical Complex for Minerals and Synthetic Substances of the University of Warsaw, using a Cameca SX 100, operating in the wavelength-dispersion (WDS) mode in the following conditions: accelerating voltage 20 kV, beam current 50 nA. Standards, analytical lines, diffracting crystals, mean detection limits (wt%) and 1σ errors (wt%) were as follows: hematite – Fe (Kα, LIF, 0.04, 0.04), rhodonite – Mn (Kα, LIF, 0.03, 0.03), pure Nb – Nb (Lα, PET, 0.05, 0.15), pure Ta – Ta (Mα, TAP, 0.03, 0.04), $Y_3Al_5O_{12}$ – Y (Lα, PET, 0.03, 0.02), orthoclase – K (Kα, PET, 0.01, 0.01) and Al (Kα, TAP, 0.01, 0.01), wollastonite – Ca (Kα, PET, 0.01, 0.02), rutile – Ti (Kα, PET, 0.02, 0.02), galena – Pb (Lα, PET, 0.10, 0.12), albite – Na (Kα, TAP, 0.01, 0.02), diopside – Mg (Kα, TAP, 0.01, 0.01) and Si (Kα, TAP, 0.02, 0.02), $SrTiO_3$ – Sr (Lα, TAP, 0.02, 0.02), cassiterite – Sn (Lα, PET, 0.04, 0.04), scheelite – W (Mα, PET, 0.03, 0.05), CeP_5O_{14} – Ce (Lα, PET, 0.05, 0.04), LaP_5O_{14} – La (Lα, PET, 0.04, 0.04),

151 REE4 – Nd (Lβ, LIF, 0.12, 0.10), REE3 – Sm (Lα, LIF, 0.08, 0.08), $Gd_3Ga_5O_{12}$ – Gd (Lα,
152 LIF, 0.07, 0.05), PrP_5O_{14} – Pr (Lβ, LIF, 0.14, 0.08), zircon – Zr (Lα, PET, 0.04, 0.04), ThO_2 –
153 Th (Mα, PET, 0.08, 0.09), UO_2 – U (Kα, TAP, 0.08, 0.10), and phlogopite – F (K_α, TAP,
154 0.10, 0.05), where REE3 and REE4 are silica glass standards, containing the respective
155 lanthanides. The data were corrected using the PAP routine (Pouchou and Pichoir 1985). The
156 correction for the interference of *REE* analytical lines was introduced using the coefficients
157 given by Reed and Buckley (1998). The chemical formulae of the pyrochlore in the analytical
158 spots were finally normalized to 2*B* atoms (B = Nb + Ta + Ti + Zr + Sn + W + $Fe^{3+(*)}$) per
159 formula unit (apfu), where $Fe^{3+(*)}$ denotes a part of total Fe shown as Fe^{3+}, determined in the
160 spot, which was related to pyrochlore based on results of single regressions between the
161 content of Si (in wt%) and the contents of Mg, Al, Fe and Mg+Al+Fe (all in wt%). The $Fe^{3+(*)}$
162 amount was calculated by diminishing of the WDS Fe content by the calculated Fe content
163 proportional to Si (the details are given in the following section). H_2O was calculated by
164 charge-balance as a supplement of $^{X}O^{2-}$ by OH^- to 6 anions pfu, assuming the F^- presence
165 only at the Y site. The calculated amount is not informative in any way on the presence of
166 molecular water that can fill the empty *Y* and *A* sites. Names of the pyrochlore species
167 corresponding to each microprobe analyse were evaluated assuming a content of the
168 molecular water in the analytical spots at most equal to the difference of the analytical total to
169 100 wt%.

170 The alpha decay dose *D* and the displacements per atom (dpa) were calculated for each
171 analytical spot on the basis of equations $D = 8N_{238}(e^{t/\tau 238}-1) + 6N_{232}(e^{t/\tau 232}-1)$, where N_{238} and
172 N_{232} denote present numbers of ^{238}U and ^{232}Th atoms/mg , τ_{238} and τ_{232} – the mean life times
173 of ^{238}U and ^{232}Th, t – the geologic age, and $dpa = 1500DM/N_tN_a$, where M denotes the
174 molecular weight in mg, N_t – the number of atoms per formula, and N_a – the Avogadro's
175 number (Lumpkin and Ewing 1988).

The TEM investigations were performed on two crystals of pyrochlore using a JEOL-JEM 2010 electron microscope operating at 200 kV, with LaB_6 source, nominal point-to-point resolution of 2.0 Å, and the spherical aberration coefficient of 0.5 mm. A double-tilt specimen holder (±20°) was used. The pyrochlore specimens for TEM observations were selected from doubly polished petrographic thin sections and fixed on the 3 mm wide copper grids. Since the pyrochlore crystals were highly fractured in thin sections, special care was taken when preparing the specimen for TEM analyses. The TEM mounts were thinned down to electron transparency by means of argon ion-milling with a Gatan PIPS system, and carbon coated to avoid an electrostatic charging inside the microscope. The TEM microanalyses were carried out using an Oxford LINK energy dispersive X-ray spectrometer (EDS) with the Si(Li) detector and ultra-thin window. The O, F, Na, Si, Ca, Ti, Fe, Nb, Ce, Ta, Th and U elements were detected and then quantified on the basis of INCA spectrum analyzer software by using theoretical k-factors. Care was taken to ensure the internal consistency of the results. The electron dose was maintained constant from place to place by using the same spot size (15 nm), acquisition time (60 s), and the mean counting rate. By using the "electron neutrality criterion" (Van Cappellen and Doukhan 1994), the chemical raw concentrations were corrected for differential absorption effects caused by variations in thickness from point to point in the analyses. Images were recorded with a Gatan MSC794 CCD camera. In order to eliminate contrasts in noise from amorphous materials, the high-resolution transmission electron microscopy (HRTEM) image was rotationally filtered (Kilaas 1998) with the HRTEM filter (Mitchell 2007), as implemented in the Gatan Digital Micrograph version 3.9 software.

The XRD and MAS-NMR studies were conducted on a pyrochlore-rich fraction, which was separated from the mariupolite. It was impossible to obtain pure pyrochlore due to its low concentration in the host rock, occurring almost always in the form of very small crystals

intergrown with albite. After cleaning, the final fraction consisted of *ca*. 90 vol.% pyrochlore and 10 vol.% albite.

The XRD patterns were recorded with a Philips PW 3020 X'Pert-APD Diffractometer system (with a Cu anode and graphite monochromator) at 35 kV voltage and 30 mA current, in the 2Θ range of 5–100^{o} with a 0.01°(2Θ)/s step. The unit-cell parameters were refined using the least squares method applying the DHN-PDS programme. A pure Si powder was used as an internal standard. The particle size was estimated from the Debye-Scherrer formula $L_{hkl}=K\alpha/\Delta B\cos\theta$, where L_{hkl} is crystallite size, K- shape factor, which typical has value of about 0.9, α - ray wavelength, ΔB the line broadening at half the maximum intensity, after subtracting the instrumental line broadening, θ - the Bragg angle.

^{29}Si solid state MAS-NMR spectra were measured on the APOLLO console (Tecmag) at the magnetic field of 7.05 T produced by the 300 MHz / 89 mm superconducting magnet (Magnex). A Bruker HP-WB high-speed MAS probe equipped with the 4 mm zirconia rotor and KEL-F cap was used to spin the sample at 4 kHz. The resonance frequency was equal to 59.515 MHz, and a single 2 μs rf excitation pulse was applied, which corresponded to about π/3 flipping angle. Due to small amount of material, the remaining space inside the rotor was filled with the Teflon cylinder, to enable a smooth spinning. The number of averages was 5300, with the acquisition delay equal to 60 s. The frequency scale in ppm was referenced to TMS (tetramethylosilane).

Results

Chemical composition

The electron-microprobe analyses of pyrochlore crystals reveal a highly diversified chemical composition (Table 1). Fluorine is present in amounts which vary randomly, from 0.00 wt% to usually higher values, up to 5.51 wt%. The main *A*-site component is Ca, with

variable amounts of Na and REEs (dominant Ce, subordinate La and Nd, with the remaining REEs present in traces only). Appreciable amounts of Th and U, which are responsible for the observed radiation damage, are ubiquitously present. The *B* site is filled mainly with Nb and, subordinately, Ti, as well as with minor, fairly constant amounts of Ta. The silicon content is found to vary from spot to spot and reaches up to 13.01 wt% SiO_2, which is one of the highest values for the pyrochlore-supergroup minerals reported in the literature. In low Si content spots, Al is completely absent; analogously, Fe and Mg contents seem to be lower when the Si concentration is very low. Correlations between the Si content and Mg, Fe and Al as the main chlorite components could reveal contamination of the pyrochlore by chlorite, after all forming common reaction rims around the pyrochlore crystals. Indeed, strong positive correlations observed for Si *vs.* Al and Si *vs.* all combinations of Al with the remaining components, e.g., Si *vs.* Al (r = 0.880), Si *vs.* Al+Mg (r = 0.897), Si *vs.* Al+Fe (r = 0.892), and Si *vs.* Al+Mg+Fe (r = 0.905) indicate that the concentration of all these minor elements, i.e. Al, Fe, Mg, can be related to the same mechanism that had enriched the pyrochlore in Si (Fig. 2). However, the components cannot be related to an external admixture of chlorite due to incompatible proportions of Si to Al, Mg and Fe and their sums, and the absence of any trace of $Q^{(3)}$ species in the MAS-NMR spectrum of the pyrochlore. Then, the *y*-intercepts close to 0.00, e.g. 0.007 wt% for Mg *vs*. Si and -0.018 wt% for Al *vs*. Si, can be accepted as analytical artefacts, but the evaluated intercept of 0.16 wt% for Fe *vs*. Si must indicate the mean statistical content of Fe in the pyrochlore structure. On the other hand, an inverse correlation is observed between Si and the Nb+Ti+Ta sum (r = -0.823), which may suggest, although not strictly prove, the incorporation of Si into the *B* site. In fact, the presence of a sub-micrometer silicate phase could also result in a negative correlation between Si and every element that is present in the pyrochlore alone. The formulae of the analyzed pyrochlore from the Mariupol massif, calculated with Si, Mg, Al, and a part of Fe correlated with Si treated as

independent components that are not related to the pyrochlore structure, are presented in Table 2.

Transmission electron microscopy

The TEM observations did not reveal any crystalline phases other than pyrochlore. This precludes hypotheses, presented earlier, that silicon present in minerals of the pyrochlore supergroup could be related to an external Si-bearing impurity (Hogarth 1989), Si in dispersed state (Voloshin et al. 1989), or intergrowths with komarovite, $(H,Ca,Na)_2(Nb,Ti)_2Si_2O_{10}(OH,F)_2$, (Chakhmouradian and Mitchell 2002). However, the examined pyrochlore crystals are inhomogeneous and show significant compositional changes related to the variation in crystallinity. The semi-quantitative TEM-EDS analyses (Table 3), as well as the selected area electron diffraction (SAED) patterns usually showed sharp variations from point to point, even though no evident microstructure was observed in the bright field (BF) images. In particular, the SAED patters taken from Si-poor areas exhibit strong and sharp diffraction spots (Fig. 3) and the Si-rich areas show weaker diffraction spots with a diffuse diffraction halo that are typical of metamict material (Fig. 4) with no apparent correlation between their distribution and the reaction border of the pyrochlore samples.

X-ray powder diffraction

In agreement with TEM observations, the XRD powder patterns for the pyrochlore display broadened reflections due to very small sizes of the crystal domains coherently scattering X-radiation (Fig. 5), which certainly resulted from the alpha-decay-induced metamictization. The estimated particle sizes, using the Debye-Scherrer formula, range from 15 nm $\perp$ (511) to 40 nm $\perp$ (100). However, it was noted that the presence of broaden reflections observed in the

XRD spectrum is not only due to the small sizes of crystallites, but also to the strain (Fig. 6). The Williamson-Hall plot presents only 5 points (assigned to full width at half maximum FWHM of 5 peaks) with quite weak regression, which seems to be due to the fact that reflections in the XRD pattern represent very weak relative intensities and the evaluation of FWHM for them is subjected to considerable inaccuracy. Moreover, the broad diffraction effects observed in the ranges of 22–38° and 48–62°(2θ) indicate the presence of almost completely metamict pyrochlore domains in the studied crystals (Lumpkin and Ewing 1988). The calculated lattice parameter for the bulk sample of the pyrochlore from mariupolite, 10.369(1) Å, is only slightly smaller than that reported in the International Centre for Diffraction Data (ICDD) for pyrochlore species with similar composition, however not containing Si (cards with no. from 85-0788 to 85-0792; 10.43 Å, 10.393 Å, 10.428 Å, 10.394 Å, 10.420 Å, respectively). It is close to the value found for the crystal from Narssârssuk, Julianehaab district, Greenland, [a = 10.3738(7) Å] containing 0.24 Si apfu (Bonazzi et al., 2006), and only slightly below the unit-cell parameter of highly metamict microlite from the Harding pegmatite [Lumpkin and Ewing 1988; Table 2 – bulk sample 288 with a = 10.389(4) Å]. However, taking into account the complexity of cation substitutions in the pyrochlore supergroup, it is hard to say whether the observed slight contraction of the cubic cell is due to the incorporation of Si^{4+} in the crystal structure or not.

Magic-Angle-Spinning Nuclear Magnetic Resonance

The ^{29}Si MAS-NMR spectrum and its deconvolution are shown in Figure 7. It is dominated by three narrow lines, representing a well ordered, crystalline phase. Both the lines positions at -93, -97 and -105 ppm and their relative intensities agree well with the literature data for albite (Smith et al. 1984). The relative contribution of these three lines to the overall spectrum equals about 70%. The remaining 30% of the NMR intensity originates from the line at -84

ppm, which is three times broader. Its line-width suggests that it represents a disordered, noncrystalline species. Generally, the tetrahedrally coordinated silicon $Q^{(n)}$ sites, where n is the number of bridging oxygens, give rise to line positions in the MAS-NMR spectrum in the -70 – -110 ppm range with respect to TMS (Bruker Almanach 2012). The shielding increases with n, but a significant overlap of the chemical shift ranges corresponding to different n prohibits a unique assignment. In extensive studies of natural silicate minerals, the chemical shift range of -75 to -95 was reported for 17 inosilicates, characterized by $Q^{(2)}$ sites (Magi et al., 1984). The lines at -90.6 and -89 ppm were found in the NMR spectra of SG-2 and S-157 silica gels, respectively (Maciel and Sindorf 1980; Sindorf and Maciel 1983). They were interpreted as $Q^{(2)}$ surface geminal-hydroxyl sites, having two siloxane bonds and two hydroxyls, $[(HO)_2\mathbf{Si}(OSi)_2]$, where the atom of interest is in bold. Based on the above literature data, the line at -84 ppm can be assigned to the $Q^{(2)}$ species, $[Si(OSi)_2(–)_2]$, corresponding to silicon atom with two bridging oxygens in the form of the cyclo- or finite-length chain-like silicon structures. Depending on the chains lengths, there will be some contribution of the $Q^{(1)}$ species, $[Si(OSi)_1(–)_3]$, corresponding to terminal Si^{4+} in the chains. They would introduce some intensity at even smaller shielding, i.e., at algebraically larger values of chemical shift, which may explain the larger line width of the observed peak and its shift toward higher field. The relative contribution of albite and $Q^{(2)}$ species in the MAS-NMR spectrum (70:30) agrees well with the chemical composition of the sample, in which the content of ^{IV}Si assigned to albite is between 60 and 70 at.%, based on the pyrochlore content in the specimen, 90 vol.%, and the mean contents of Si in the albite and the pyrochlore. It should be also noted that neither the line at about -200 ppm, which would correspond to the sixfold-coordinated silicon species (Stebbins and Kanzaki 1991) as suggested by Bonazzi et al. (2006), nor the line at -75 ppm that was found in the synthesized

pyrochlore by Luca et al. (2005) and interpreted as isolated $Si(OH)_4$ species [$Q^{(0)}$] located within the hexagonal channels of the pyrochlore framework are observed in the present study.

Discussion

Alteration effects

The compositions of the Mariupol pyrochlore plot as two separate subsets grouped along the lines of constant 20 and 40 Ca at.% of the *A* site, in the ternary Ca^{2+} – Na^{+} – $^{A}\square$ diagram (Fig. 8a). It was recommended by Lumpkin and Ewing (1995) as one of the compositional methods to discriminate between the primary, transitional and secondary alterations in minerals of the supergroup. Both paths are parallel to the trend of transitional alteration by Lumpkin and Ewing (1995) or of hydrothermal pyrochlores by Nasraoui and Bilal (2000), although they are located somewhat above them. The path closer to the *A*-site vacancy corner corresponds to Si-free and Si-poor domains, particularly in the core crystals. The second path pointing towards the centre of the ^{A}Ca – *A*-site vacancy side ($\square CaNb_2O_6\square$) matches the Si-enriched patches and the outer crystals rims. The compositions of pyrochlore in the Si-free – Si-poor branch vary from Na- and F-rich close to $^{A}(Na_{1.0}Ca_{0.2}REE_{0.2}\square_{0.6})^{B}(Nb,Ti,Ta,Fe^{3+})_2{}^{X}(O_{5.1}OH_{0.9})^{Y}(F_{0.8}\square_{0.2})$, to Na-poor, F-bearing and Na-poor, F-poor, corresponding to $^{A}(Na_{0.1}Ca_{0.2}REE_{0.3}A_{0.1}\square_{1.3})^{B}(Nb,Ta,Ti,Fe^{3+})_2{}^{X}(O_{4.6}OH_{1.5})^{Y}(F_{0.6}\square_{0.4})$ and $^{A}(Ca_{0.4}REE_{0.3}A_{0.1}\square_{1.2})^{B}(Nb,Ta,Ti,Fe^{3+})_2{}^{X}(O_{5.7}OH_{0.3})^{Y}(F_{0.1}\square_{0.9})$, respectively, where *A* = Mn+Sr+Pb+U+Th. The pyrochlore in the Si-enriched domains varies from Na- and F-rich variety $^{A}(Na_{1.0}Ca_{0.6}REE_{0.1}\square_{0.3})^{B}(Nb,Ti,Ta,Fe^{3+})_2{}^{X}(O_{5.7}OH_{0.3})^{Y}F_{1.0}$ through Na-poor, F-bearing $^{A}(Na_{0.1}Ca_{0.7}REE_{0.2}A_{0.1}\square_{0.9})^{B}(Nb,Ta,Ti,Fe^{3+})_{2.0}{}^{X}O_{6.0}{}^{Y}(F_{0.2}OH_{0.1}\square_{0.7})$, to almost Na- and F-free close to $^{A}(Ca_{0.5}REE_{0.2}A_{0.2}\square_{1.1})^{B}(Nb,Ta,Ti,Fe^{3+})_{2.0}{}^{X}O_{6.0}{}^{Y}(OH_{0.1}\square_{0.9})$. At the first sight the pyrochlore compositions of the two subsets seem surprising, because the 'altered' Si-rich pyrochlore has smaller number of vacancies than its Si-free to Si-negligible counterparts. It

would be rather expected that the compositions corresponding to the 'altered' Si-rich domains should have more vacancies. This apparently nonphysical result can be explained on the basis of the known models of the primary and secondary alterations in minerals representing the pyrochlore group (Lumpkin and Ewing 1995), running along with metamictization, which additionally may favour geochemical modifications in the minerals. The occurrence of the pyrochlore in mariupolite, mostly in the interstices between the albite crystals, as well as its overgrowth with the undoubtedly hydrothermal Fe-bearing chlorite indicate the late-magmatic to early-hydrothermal origin of the mineral. After crystallization, probably as a U- and Th-bearing, partly *A*-site vacant species, the mineral was affected by a fluid phase that is typical of nepheline syenites, and independently at the same time reconstructed its structure as a result of progressive metamictization. Its initial alterations at high temperature were connected with the ${}^{A}\mathrm{Na}^{Y}\mathrm{F} \rightarrow {}^{A}\square^{Y}\square$ substitution under conditions of weakly-acidic fluid phase, moderate a_{HF} and high $a_{\mathrm{Si4+}}$. The domains compositions of the pyrochlore crystals differentiated mainly with respect to Na and F contents, and the number of vacancies at the *A* and *Y* sites. Taking into account the elevated number of hydroxyls at the *X* site, a part of Na was probably lost by the ${}^{A}\mathrm{Na} + {}^{X}\mathrm{O} \rightarrow {}^{A}\square + {}^{X}\mathrm{OH}$ substitution that affected the first coordination sphere around the *B* cations. Along with the evolution of the fluid phase toward more basic with low and very low a_{HF} and high $a_{\mathrm{Ca2+}}$, the ${}^{A}\square^{Y}\square \rightarrow {}^{A}\mathrm{Ca}^{Y}\mathrm{O}$ and ${}^{A}\mathrm{Na}^{Y}\mathrm{F} \rightarrow {}^{A}\mathrm{Ca}^{Y}\mathrm{O}$ substitutions dominated, and a part of the *A*-site vacancies was filled in the secondary process by cations (mainly Ca^{2+}, but also Mn^{2+}, Sr^{2+}, K^{+},…), provided by the fluids, enriched in these elements by interaction with mineral components of the host rock. The high Ca^{2+} activity in this stage was the main reason for the shift of the pyrochlore compositions to the left, toward the Ca^{2+} corner of the $Ca^{2+} - Na^{+} - {}^{A}\square$ triangle, corresponding to the $Ca_2Nb_2O_7$ end-member. This is corroborated by *ca*. twice greater content of Ca in the Si-bearing spots than in the spots showing only a minor Si content. The contents of the trace elements like Mn,

374 Sr, K, U and Th, as well as the Y/Ce ratio are also about two times greater (in the case of Sr
375 even several times greater) in the Si-rich domains. Such pattern is consistent with the
376 geochemical characteristics of primary alterations that were defined by Lumpkin and Ewing
377 (1996). The progressive decrease in acidity of the fluids carrying silica acid resulted in the
378 precipitation of a $Q^{(2)}$ Si-bearing species, which was only possible in the severely damaged
379 portions of the structure. The primary alterations induced by high-temperature, Ca^{2+}-and Si^{4+}-
380 rich fluids are not observed in the bulk volume of the pyrochlore grain but only in the
381 irregular, Si-enriched patchy domains. The remaining parts of the grains with none or only
382 minor Si visible under EMP were not altered at this stage.
383 The secondary alterations could be induced by the exposure of the rock to ground water
384 with relatively high acidity at the temperature below 150 ^{o}C. These processes affected the
385 bulk volume of the pyrochlore grains, so they overprinted the domains with the primary
386 alteration signature as well, showing the Si enrichment. Under such conditions coupled
387 dissolution-reprecipitation process (Geisler et al., 2005) could lead to the leaching of some the
388 *A*- and *Y*-site components by the $^{A}Na^{Y}F \rightarrow {}^{A}\square^{Y}\square$ and $^{A}Ca^{Y}O \rightarrow {}^{A}\square^{Y}\square$ substitutions both in
389 the parts of the grains with signs of the primary alteration (Lumpkin and Ewing, 1996;
390 Nasraoui and Bilal 2000), as well as in those that were earlier unaffected. This process
391 resulted in a higher number of the *A*-site vacancies in only secondary-altered parts of the
392 grains than in those affected by both primary and secondary alteration processes (Fig. 8b).
393
394 *Metamictization effects*
395 The ^{29}Si MAS-NMR analyses and, in particular, the lack of any ^{29}Si MAS-NMR resonance
396 close to -200 ppm, where the $^{VI}Si^{4+}$ should manifest, exclude the presence of Si^{4+} at the
397 typical *B* site of the pyrochlore structure in the studied material. Since no intergrowth with
398 other Si-bearing phases was observed in the TEM images, even at high magnification, it

399 seems reasonable to conclude that Si^{4+} can occupy severely damaged portions of this
400 structure, possibly as bridging silicon tetrahedra. According to Lumpkin and Ewing (1988),
401 the structure of pyrochlore in the metamictic state can be envisioned as an aperiodic, random
402 network of corner sharing *B*-O polyhedra. The XRD and EXAFS/XANES (X-ray Absorption
403 Fine Structure/X-ray Absorption Near Edge Spectroscopy) data (Greegor et al. 1985a; 1985b;
404 1987) are consistent with a slight decrease in <*B*-O> during the transition from crystalline to
405 the metamictic state accompanied by an increased distortion and a reduction in average
406 coordination number to about 5.5. Thus, it can be reasonably hypothesized that the
407 environment around a certain number of *B* sites could collapse to 5 or even to 4, i.e., a
408 coordination more suitable for silicon than the octahedral one, however, no other Si
409 coordination than tetrahedral was confirmed by the presence of respective lines in the
410 recorded MAS-NMR spectrum. On the other hand, the reconstruction of the pyrochlore
411 structure from the crystalline to the metamict state connected with largely disrupted
412 periodicity beyond the first coordination sphere (Greegor et al. 1985; 1987), should very
413 likely be coupled with the alpha-decay-induced damage of continuity in the net of *B*
414 polyhedra, and with the changes around the *A* sites as well. This fact might concur with the
415 increase of the mean diameter of hexagonal tunnels around the empty *A* sites (in the
416 crystalline pyrochlore typically about 2.6 Å), making possible their filling by the corner-
417 shared Si tetrahedra in $Q^{(2)}$ with subordinate $Q^{(1)}$ structures. The occasional presence of rather
418 small amounts of silicon in some other U- and Th-rich Nb-Ta oxides, like these representing
419 the samarskite or euxenite groups, points to the role of metamictization in the Si incorporation
420 into the structures. The pyrochlore-supergroup minerals, however, due to their simultaneous
421 compliance with the Schottky defect induced by chemical alteration, and the structure
422 reconstruction towards the metamict state, seem to be exceptionally susceptible to the Si
423 incorporation. The simultaneous contribution of metamictization and geochemical alteration

processes in the incorporation of Si into pyrochlore is corroborated by the correlation between the SiO_2 content at analyzed spots and the calculated alpha-decay dose (Fig. 9). Comparable ranges of the dose (or *dp*a) for Si-poor and Si-rich domains, 3.5–9.5 $\cdot 10^{16}$ alpha-events/mg (*dpa* ≈ 3.1–9.0) and 1.0–13.5 $\cdot 10^{16}$ alpha-events/mg (*dpa* ≈ 0.9–12.8), respectively, suggests that metamictization alone does not favour the Si incorporation. The interplay of both processes, i.e., metamictization and geochemical alteration, is also proved both by low Si amounts in U- and Th-free, altered pyrochlore species (e.g., Pieczka 2010, Table 8), as well as by very high Si contents observed in strongly altered and completely or at least partly metamicted ones. A high metamictization degree of the mariupolite's pyrochlore, rather poor in UO_2 and ThO_2 (only 1.41 and 0.88 wt% as the mean contents, respectively) is reflected in a relatively high mean dose value of 7.35 $\cdot 10^{16}$ alpha-events/mg and mean *dpa* close to 6.66. The alpha-decay doses corrected for annealing of alpha-recoil tracks, with assumption of a mean alpha-recoil track life τ_a = 100 Ma (for more information see Lumpkin and Ewing 1988) characterize a mean value of 0.64 $\cdot 10^{16}$ alpha-events/mg that locates the mariupolite's pyrochlore relatively close to fully-metamict species, with strongly decreased intensities I/I_0 in X-ray diffraction. A decisive feature responsible for the current pattern of the pyrochlore is its geological age of 1.8 Ga, older than many other partly- or fully-metamicted pyrochlore species known in literature (cf., Lumpkin and Ewing 1988).

We are aware that problem is not solved definitively. Additional investigations of Si-rich pyrochlore by advanced TEM methods, like High-Resolution Scanning-Transmission – High-Angle Annular Dark-Field (HRSTEM-HAADF) imaging utilizing Z-contrast and chemical element mapping and high-resolution elemental mapping in EFTEM mode **(**Energy-Filtered Transmission Electron Microscopy) are planned in the future.

Implications

Our studies of a *silicified* pyrochlore from mariupolite (aegirine-albite nepheline syenite) of the Mariupol massif (Ukraine) excluded the presence of 6-fold coordinated Si^{4+} at the *B* site of the pyrochlore structure, or an external admixture of a silicate phase. We found that Si present in the pyrochlore occurs in the form of $Q^{(2)}$ species, $[Si(OSi)_2(-)_2]$, corresponding to Si atom with two bridging oxygens, forming finite-length chain-like or cyclo-silicon structures in damaged by alteration and metamictization portions of the structure. The alpha-decay-induced metamictization could damage the continuity of the *B* octahedra net, reducing the effective coordination number around the sites, while geochemical alteration induced the Schottky deffects at the *A* and *Y* sites; both effects could intensify mutually and favour deposition of Si. This implicates the presence of Si^{4+}, e.g., by leaching of the host silicate minerals, and its significant role in high-temperature juvenile fluids with high pH, high Na- and Ca activities, derived from high-level alkaline magmatic complexes. These fluids could cause subsolidus alterations connected with Si diffusion in damaged portions of the pyrochlore structure during the immediate post-magmatic stage in the nepheline syenite of the Mariupol Massif. The accommodation of Si by altered and metamicted pyrochlore can be an important sign of the processes chemistry, and *silicified* pyrochlore can be used as useful indicator. However, our studies are based only on one variety of a species representing the pyrochlore supergroup; we are aware that problem is not solved definitively. Therefore, additional investigations of various Si-rich pyrochlore species by advanced TEM on more homogenous and bigger grains of Si-enriched pyrochlore-supergroup minerals from other localities should be planned in the future.

Finally, understanding the role and the localization of Si in the *silicified* pyrochlore structure is crucial for calculation its chemical formula and classification of the pyrochlore supergroup. The absence of Si at the *B* site suggests that formulae should be calculated by the simple normalization of analyses to 2*B* apfu without Si. It is the only realistic approach,

474 which is similar to the one proposed by Ercit et al. (1993), commonly used for typical,
475 nonsilicified pyrochlore species. The final recognition of Si^{4+} role in the pyrochlore structure
476 can eliminate the postulated existence within the pyrochlore supergroup of a new pyrochlore
477 group with Si^{4+} dominant at the *B* site. This is especially important for many altered ±
478 metamicted natural samples, in which the SiO_2 content attains even close to 20 wt%.
479

480 **Acknowledgements:** The paper benefitted from constructive comments of the reviewers and
481 editors of American Mineralogist: Daniel Atencio, Greg Lumpkin, and Keith Putrika, Joshua
482 Feinberg. We also sincerely thank Paola Bonazzi for her stimulating criticism, friendly
483 comments and discussion on the early version of the manuscript. Edward S. Grew, Sergey N.
484 Britvin and Aleksandra Czyrska-Filemonowicz are thanked for reading the manuscript and
485 their helpful remarks. We gratefully acknowledge the help of Mateusz Rechowicz and Adam
486 Gaweł for the separation of a pyrochlore-rich fraction from mariupolite and the assistance
487 with X-ray studies and the calculation of the unit-cell parameter of the pyrochlore,
488 respectively. The work was financially supported by the AGH University of Science and
489 Technology (Krakow, Poland) statutory research project no 11.11.140.319
490

491 **References**

492 Atencio, D., Andrade, M.B., Christy, A.G., Gierè, and Kartashov, P.M. (2010) The
493 pyrochlore supergroup of minerals: nomenclature. The Canadian Mineralogist, 48, 673-
494 698.
495 Balić-Žunić, T., Petersen, O.V., Bernhardt, H.J., and Micheelsen, H.I. (2002) The crystal
496 structure and mineralogical description of a Na-dominant komarovite from the Ilímaussaq

497 alkaline complex, South Greenland. Neues Jahrbuch für Mineralogie Monatshefte, 11, 497-
498 514.
499 Bonazzi, P., Bindi, L., Zoppi, M., Capitani, G.C., and Olmi F. (2006) Single-crystal
500 diffraction and transmission electron microscopy studies of "silicified" pyrochlore from
501 Narssârssuk, Julianehaab district, Greenland. American Mineralogist, 91, 794-801.
502 Brugger, J., Gierè, R., Graeser, S., and Meisser, N. (1997). The crystal chemistry of romèite.
503 Contributions to Mineralogy and Petrology, 127, 136-146.
504 Bruker Almanach 2012, T18.
505 Chakhmouradian, A.R. and Mitchell, R.H. (2002) New data on pyrochlore- and perovskite-
506 group minerals from the Lovozero alkaline complex, Russia. European Journal of
507 Mineralogy, 14, 821-836.
508 Donskoy, A.N. (1982) The nepheline complex of alkaline Oktyabr'skii massif, 150p. The
509 Ukrainian Academy of Science, Kiev, (in Ukrainian).
510 Dumańska-Słowik, M., Baranov, P., Heflik, W., Natkaniec-Nowak, L, Shevchenko, S., and
511 Tsotsko, L.I. (2011a) Mariupolite from the Oktyabrsky Massif (SE Ukraine)- a less known
512 rock in the gemstone trade. Zeitschrift der Deutschen Gemmologichen Gesellschaft, 60(1-
513 2), 37-48.
514 Dumańska-Słowik, M.,Sikorska, M., and Heflik, W. (2011b) Dissolved-recrystallized zircon
515 from mariupolite in the Mariupol Massif, Priazovje (SE Ukraine). Acta Geologica
516 Polonica, 61(3), 277-288.
517 Dumańska-Słowik, M., Budzyń, B., Heflik, W., and Sikorska, M. (2012) Stability
518 relationships of REE-bearing phosphates in an alkali-rich system (nepheline syenite from
519 the Mariupol Massif, SE Ukraine). Acta Geologica Polonica, 62(2), 247-265.
520 Ercit, T.S., Černý, P., and Hawthorne, F.C. (1993) Cesstibtantite - a geologic introduction to
521 the inverse pyrochlores. Mineralogy and Petrology, 48, 235-255.

Ferraris, G., Makovicky, E., and Merlino, S. (2004) Crystallography of modular materials. IUCr Monographs on Crystallography 15, Oxford University Press. USA.

Geisler, T., Seydoux-Guillaume, A.-M., Poeml, P., Golla-Schindler, U., Berndt, J., Wirth, R., Pollok, K., Janssen, A., Putnis, A. (2005). Experimental hydrothermal alteration of crystalline and radiation-damaged pyrochlore. Journal of Nuclear Materials, 344(1-3), 17-23.

Greegor, R.B., Lytle, F.W., Chakoumakos, B.C., Lumpkin, G.R., and Ewing, R.C. (1985a). An investigation of metamict and annealed pyrochlores by x-ray absorption spectroscopy. In: Jantzen, C.M., Stone, J.A., and Ewing, R.C. (eds). Scientific Basis for Nuclear Waste Management VIII, Materials Research Society, Pittsburgh, 655-662.

Greegor, R.B., Lytle, F.W., Chakoumakos, B.C., Lumpkin, G.R., and Ewing, R.C. (1985b). An investigation of uranium L-edges of metamict and annealed betafite. In: Werme, L.O. (eds). Scientific Basis for Nuclear Waste Management IX, Materials Research Society, Pittsburgh, 387-392

Greegor, R.B., Lytle, F.W., Chakoumakos, B.C., Lumpkin, G.R. Ewing, R.C., Spiro, C.L., and Wong, J. (1987). An x-ray absorption spectroscopy investigation of the Ta site in alpha-recoil damaged natural pyrochlores. In: Bates, J.K., and Seefeldt, W.B. (eds). Scientific Basis for Nuclear Waste Management X, Materials Research Society, Pittsburgh, 645-658.

Hogarth, D.D. (1989) Pyrochlore, apatite and amphibole: distinctive minerals in carbonatite. pp. 105-148 in Carbonatites: *Genesis and Evolution* (K. Bell, editor). Unwin Hyman Ltd., London.

Kilaas, R. (1998) Optimal and near-optimal filters in high-resolution electron microscopy. Journal of Microscopy, 190, 45-51.

Krivdik, S.G., Nivin, V.A., Kul'chitskaya, A.A., Voznak, D.K., Kalinichenko ,A.M., Zagnitko, V.N. and Dubyna, A.V. (2007) Hydrocarbons and other volatile components in alkaline rocks from the Ukrainian Shield and Kola Penisula. Geochemistry International, 45(3), 270-294.

Krivokoneva, G.K., Portnov, A.M., Semenov, E.I,. and Dubakina, L.S. (1979) Komarovite – silicified pyrochlore. Doklady AN SSSR, Earth Science Section, 248, 127-130.

Luca, V., Griffith, C.S., Blackford, M.G., and Hanna, J.V. (2005) Structural and ion exchange properties of nanocrystalline Si-doped antimony pyrochlore. Journal of Materials Chemistry, 15, 564-572.

Lumpkin, G.R. and Ewing, R.C. (1988) Alpha-decay damage in minerals of the pyrochlore group. Physics and Chemistry of Minerals, 16, 2-20.

Lumpkin, G.R. and Ewing, R.C. (1995) Geochemical alteration of pyrochlore group minerals: pyrochlore subgroup. American Mineralogist, 80, 732-743.

Lumpkin G.R. and Ewing R.C. (1996) Geochemical alteration of pyrochlore group minerals: Betafite subgroup. American Mineralogist, 81**,** 1237-1248.

Maciel, G. E. and Sindorf, D.W (1980) Silicon-29 Nuclear Magnetic Resonance Study of the Surface of Silica Gel by Cross Polarization and Magic-Angle Spinning. Journal of The American Chemical Society, 102, 7607-7608.

Magi, M., Lippmaa, E., Samoson, A., Engelhardt, G., and Grimmer, A. (1984) Solid-state high- resolution silicon-29 chemical shifts in silicates. Journal of Physical Chemistry, 88, 1518-1522.

Mitchell, D.R.G. (2007) HRTEM filter. Digital_Micrograph_Script_ Database. http://www.felmpc14.tu-graz.ac.at/ dm_scripts/ freeware / programs/ hrtem_ filter.htm.

Nasraoui, M. and Bilal, E.(2000) Pyrochlores from Lueshe carbonatite complex (Democratic

Republic of Congo): a geochemical record of different alteration stages. Journal of Asian Earth Sciences, 18, 237-251.

Pieczka, A. (2010) Primary Nb-Ta minerals in the Szklary pegmatite, Poland: New insight into controls of crystal chemistry and crystallization sequences. American Mineralogist, 95, 1478-1492.

Pouchou, I. L, and Pichoir, F. (1985) "PAP" (phi-rho-z) procedure for improved quantitative microanalysis. Pp. 104-106 in: *Microbeam Analysis* (Armstrong IT, editor). San Francisco Press, San Francisco.

Sindorf , D.W. and Maciel, G. E (1983) ^{29}Si NMR Study of Dehydrated/Rehydrated Silica Gel Using Cross Polarization and Magic-Angle Spinning. Journal of The American Chemical Society, 105, 1487-1493.

Smith, J. V., Blackwell, C.S., and Hovis, G.L. (1984) NMR of albite-micro-cline series, Nature, 309, 140-142.

Stebbins, J.F. and Kanzaki, M. (1991) Local structure and chemical shifts for six-coordinated silicon in high-pressure mantle phases. Science, 251, 294.

Van Cappellen, E. and Doukhan, J.-C. (1994) Quantitative transmission X-ray microanalysis of ionic compounds. Ultramicroscopy, **53**, 343-349.

Volkova, T.P. (2000) The genesis and ore mineralization of alkaline rocks from the Oktyabr'skii Massif. Sbornik Nauchnykh Trudov, 4, 9-10 (in Ukrainian).

Volkova, T.P. (2001) The productivity criterion of REE and ore mineralization within rocks of the Oktyabr'skii Massif . Naukovi praci DonDTU, 36, 63-69 (in Ukrainian).

Voloshin, A.V., Pakhomovskiy, Ya.A., Pushcharovskiy, D.Yu., Nadezhina, T.N., Bakhchisaraitsev, A.Yu., and Kobyashev, Yu.S. (1989) Strontiopyrochlore: composition and structure. Trudy Mineralogicheskogo Muzeya AN SSSR, 36, 12-24 (in Russian).

Wall, F., Williams, C.T., Woolley, A.R. and Nasraoui, M. (1996) Pyrochlore from weathered carbonatite at Lueshe, Zaire. Mineralogical Magazine, 60, 731-750.

599 **Figure captions**

600 **Figure 1**. Backscattered electron images (BSE) of pyrochlore crystals from the Mariupol
601 massif with traces of oscillatory zoning and irregular alteration patches.

602 **Figure 2.** Covariations of Si vs (a) Mg, (b) Al, (c) Fe, (d) Mg+Al+Fe, (e) Ti+Nb+Ta (all
603 components in wt%). The error bars are comparable with the symbols.

604 **Figure 3.** High crystallinity, Si-poor areas. (a) [110] SAED pattern, (b) [110] HRTEM image,
605 (c) EDS spectrum, (d) [110] BF image.

606 **Figure 4.** Low crystallinity, Si-rich areas. (a) [111] SAED pattern, (b) EDS spectrum, (c)
607 [111] BF image.

608 **Figure 5.** A fragment of X-ray powder diffraction pattern of pyrochlore-rich fraction from
609 mariupolite.

610 Figure 6. Williamson-Hall plot of pyrochlore from *mariupolite*.

611 **Figure 7**. ^{29}Si MAS NMR spectrum of pyrochlore-rich fraction.

612 **Figure 8**. (a) Alteration trends in crystals of pyrochlore from *mariupolite* in the triangle Na –
613 Ca – A-site vacancy. (b) Vector interpretation of the alteration trends: P1and P2 – trends
614 related to the primary alterations; S – trend of secondary alterations.

615 **Fig. 9.** Plot of SiO_2 (wt%) versus alpha-decay dose (alpha-events/mg). The error bars are
616 smaller than the symbols.

617

618 **TABLES**

619**Table 1**. Representative EMPA compositions of pyrochlore from the Mariupol Massif

620**Table 2.** Representative formulae of pyrochlore from the the Mariupol massif

621**Table 3.** Semiquantitative EDX-TEM elemental chemical composition (wt% element).

622

Table 1. Representative EMPA compositions of pyrochlore from the Mariupol Massif

	1	2	3	4	5	6	7	8	9	10
wt.%										
WO_3	0.36	0.47	0.74	0.48	0.64	0.00	0.61	0.33	0.50	0.34
Nb_2O_5	59.81	50.80	58.29	49.75	48.11	56.99	56.49	56.05	61.18	57.95
Ta_2O_5	2.20	6.15	3.30	6.78	4.87	0.50	3.15	5.64	2.43	2.22
SiO_2	0.13	8.90	0.00	9.43	11.36	13.01	0.06	4.75	0.17	0.10
TiO_2	7.86	7.81	8.07	6.17	5.71	2.78	7.76	6.49	6.26	8.84
ZrO_2	0.32	0.49	0.24	2.03	0.22	0.10	0.28	0.31	0.20	0.34
SnO_2	0.20	0.54	0.34	0.62	0.43	0.26	0.23	0.55	0.24	0.06
ThO_2	1.47	0.49	0.92	1.55	1.26	0.11	0.91	0.36	0.81	1.59
UO_2	0.70	1.74	1.64	2.05	2.77	0.23	1.62	3.14	0.85	0.54
Al_2O_3	0.02	0.13	0.00	0.59	1.15	0.53	0.00	0.04	0.00	0.00
Fe_2O_3	0.19	1.01	0.17	0.91	0.98	2.62	0.11	0.74	0.10	0.09
Y_2O_3	0.29	0.15	0.30	0.22	0.11	0.10	0.24	0.39	0.32	0.09
La_2O_3	1.91	1.02	2.43	1.28	0.93	0.07	2.12	1.68	2.11	2.16
Ce_2O_3	5.36	2.58	6.20	3.68	2.20	0.24	5.56	4.60	5.46	5.87
Pr_2O_3	0.48	0.00	0.81	0.34	0.25	0.00	0.42	0.23	0.69	0.65
Nd_2O_3	1.82	0.89	2.03	1.32	0.55	0.00	1.98	1.63	1.59	2.15
Sm_2O_3	0.24	0.26	0.37	0.26	0.00	0.13	0.24	0.27	0.17	0.36
Gd_2O_3	0.67	0.37	0.74	0.38	0.31	0.00	0.63	0.50	0.50	0.85
MgO	0.00	0.27	0.00	0.13	0.10	0.00	0.00	0.00	0.00	0.00
CaO	2.80	8.60	3.11	8.51	10.17	13.99	5.36	6.21	5.08	1.99
MnO	0.09	0.45	0.30	0.27	0.22	0.18	0.15	1.01	0.00	0.10
SrO	0.00	1.03	0.00	0.72	1.01	0.21	0.11	0.43	0.11	0.00
PbO	0.00	0.08	0.00	0.06	0.17	0.05	0.00	0.09	0.08	0.11
Na_2O	8.34	0.24	0.82	0.13	0.19	2.90	2.55	0.16	5.39	8.92
K_2O	0.00	0.28	0.27	0.07	0.07	0.74	0.04	0.57	0.00	0.03
F	4.13	0.77	2.87	0.44	0.97	3.55	3.31	0.19	3.99	3.93
-O=F	-1.74	-0.32	-1.21	-0.19	-0.41	-1.49	-1.39	-0.08	-1.68	-1.66
$H_2O_{(calc.)}$	2.53	1.59	3.47	0.89	0.45	0.58	2.59	1.19	2.35	2.41
Total	100.19	96.77	96.23	98.88	94.78	98.36	95.16	97.48	98.88	100.03

Notes: H_2O was calculated by stoichiometry as a supplement of $^{X}O^{2-}$ by OH^{-} to 6 anions pfu, assuming the F presence only at the Y site.

Table 2. Representative formulae of pyrochlore from the the Mariupol massif

	1	2	3	4	5	6	7	8	9	10
a.p.f.u.										
Th^{4+}	0.020	0.007	0.012	0.023	0.021	0.002	0.013	0.005	0.011	0.021
U^{4+}	0.009	0.025	0.022	0.030	0.044	0.004	0.022	0.043	0.011	0.007
Y^{3+}	0.009	0.005	0.010	0.008	0.004	0.004	0.008	0.013	0.010	0.003
La^{3+}	0.042	0.024	0.053	0.031	0.025	0.002	0.048	0.038	0.047	0.047
Ce^{3+}	0.116	0.061	0.135	0.089	0.058	0.006	0.125	0.105	0.120	0.127
Pr^{3+}	0.010	0.000	0.017	0.008	0.006	0.000	0.009	0.005	0.015	0.014
Nd^{3+}	0.038	0.020	0.043	0.031	0.014	0.000	0.044	0.036	0.034	0.046
Sm^{3+}	0.005	0.006	0.008	0.006	0.000	0.003	0.005	0.006	0.004	0.007
Gd^{3+}	0.013	0.008	0.015	0.008	0.007	0.000	0.013	0.010	0.010	0.017
Ca^{2+}	0.177	0.593	0.198	0.601	0.784	1.060	0.353	0.413	0.327	0.126
Mn^{2+}	0.005	0.025	0.015	0.015	0.013	0.011	0.008	0.053	0.000	0.005
Sr^{2+}	0.000	0.038	0.000	0.028	0.042	0.008	0.004	0.015	0.004	0.000
Pb^{2+}	0.006	0.008	0.012	0.009	0.012	0.000	0.010	0.006	0.008	0.005
Na^{+}	0.955	0.030	0.095	0.017	0.026	0.397	0.304	0.019	0.628	1.025
K^{+}	0.000	0.023	0.020	0.006	0.007	0.067	0.003	0.045	0.000	0.003
Σ A site	1.404	0.874	0.654	0.910	1.064	1.564	0.969	0.813	1.229	1.454
W^{6+}	0.003	0.009	0.005	0.011	0.008	0.005	0.004	0.009	0.004	0.001
Nb^{5+}	1.595	1.478	1.566	1.484	1.564	1.822	1.571	1.572	1.662	1.553
Ta^{5+}	0.035	0.108	0.053	0.122	0.095	0.010	0.053	0.095	0.040	0.036
Ti^{4+}	0.349	0.378	0.361	0.306	0.309	0.148	0.359	0.303	0.283	0.394
Zr^{4+}	0.009	0.015	0.007	0.065	0.008	0.003	0.009	0.009	0.006	0.010
Sn^{4+}	0.000	0.002	0.000	0.002	0.005	0.001	0.000	0.002	0.002	0.003
Fe^{3+}	0.008	0.010	0.008	0.011	0.011	0.011	0.005	0.010	0.005	0.004
Σ B site	2.000	2.000	2.000	2.000	2.000	2.000	2.000	2.000	2.000	2.000
O^{2-}	5.002	5.319	4.624	5.609	5.784	5.724	4.936	5.509	5.060	5.048
$OH^{-}_{(calc.)}$	0.998	0.681	1.376	0.391	0.216	0.276	1.064	0.491	0.940	0.952
F^{-}	0.771	0.157	0.539	0.092	0.221	0.794	0.644	0.037	0.758	0.737
Si^{4+}*	0.008	0.573	0.000	0.622	0.817	0.920	0.004	0.295	0.010	0.006
Al^{3+}*	0.001	0.010	0.000	0.046	0.098	0.044	0.000	0.003	0.000	0.000
Mg^{2+}*	0.000	0.025	0.000	0.013	0.011	0.000	0.000	0.000	0.000	0.000
Fe^{3+}*	0.000	0.039	0.000	0.035	0.042	0.128	0.000	0.025	0.000	0.000
D	4.8	8.1	8.2	10.7	13.5	1.1	8.1	14.1	4.6	4.2
dpa	4.1	7.5	7.6	10.3	12.7	0.9	7.4	13.6	4.1	3.7

Notes: formulae were normalized in relation to **Σ**B = 2 a.p.f.u.; OH^{-} was calculated by stoichiometry as a supplement of $^{X}O^{2-}$ by OH^{-} to 6 anions pfu, assuming the F presence only at the Y site;* - an impurity not related to the pyrochlore structure. Abbreviations: D – alpha decay dose (10^{16} alpha-events/mg), dpa – displacements per atom. Evaluated names of the pyrochlores: 1, 10 – fluornatropyrochlore; 2 – hydrokeno- to kenopyrochlore; 3 – fluorkeno- to flluorhydropyrochlore, 4 – hydroxykeno- to kenopyrochlore; 5 – hydrocalcio- to hydropyrochlore; 6 – fluorcalciopyrochlore; 7 – fluorhydropyrochlore; 8 – hydrokeno- to kenopyrochlore; 9 – fluornatro- to fluorkenopyrochlore;

Table 3. Semiquantitative EDX-TEM elemental chemical composition (wt.% element)

	Si-poor areas		Si-rich areas	
	range	mean (no.*=5)	range	mean (no.*=4)
O	21.82-33.85	26.75	30.53-34.38	32.07
F	1.20-2.82	0.62	-	-
Na	4.73-6.05	5.17	3.41-4.60	4.15
Si	1.87-2.44	2.10	4.00-5-08	4.54
Ca	6.46-7.79	7.27	5.52-7.42	6.72
Ti	4.28-5.31	4.84	3.52-4.28	3.79
Fe	0.66-1.15	0.87	1.12-1.71	1.48
Nb	37.93-46.87	42.86	34.99-36.13	35.73
La	0.00-1.32	0.81	0.30-3.79	1.52
Ce	4.34-5.86	5.15	1.97-3.72	2.67
Ta	1.09-1.86	1.41	3.75-5.52	4.81
Th	0.11-0.66	0.42	0.00-1.50	0.31
U	0.05-1.32	0.46	1.05-3.48	2.21

*Number of analyses

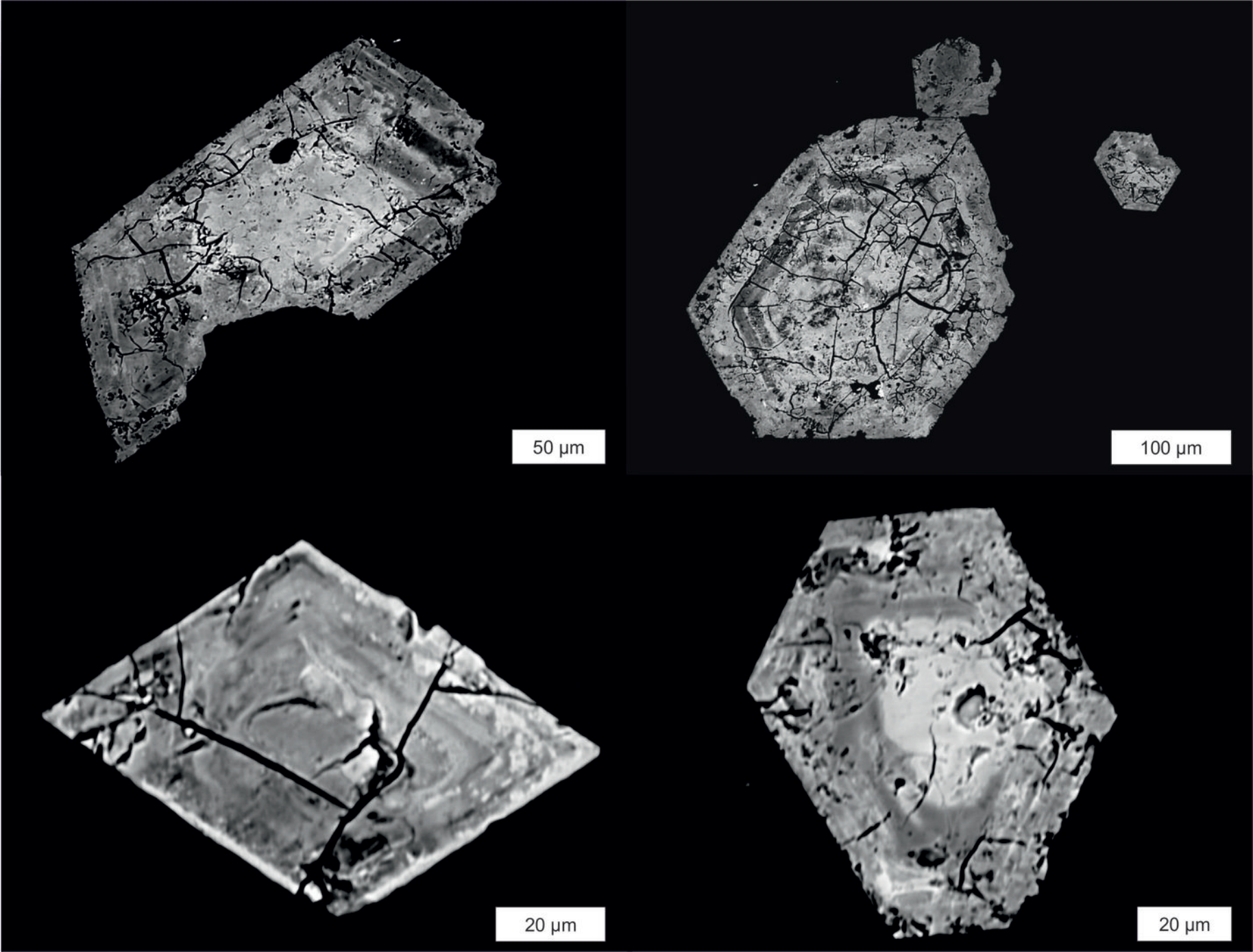
50 µm
100 µm
20 µm
20 µm

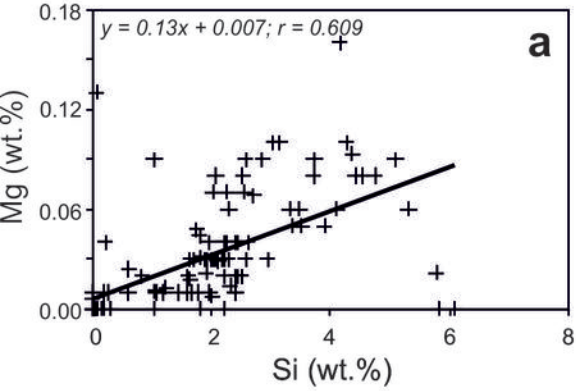
y = 0.13x + 0.007; r = 0.609
a
Mg (wt.%)
Si (wt.%)
0.18
0.12
0.06
0.00
0
2
4
6
8

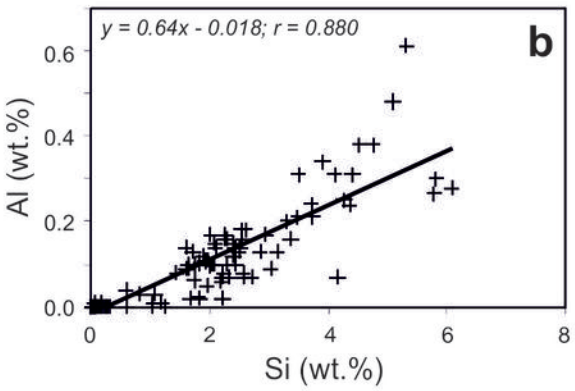
y = 0.64x - 0.018; r = 0.880
b
Al (wt.%)
Si (wt.%)
0.6
0.4
0.2
0.0
0
2
4
6
8

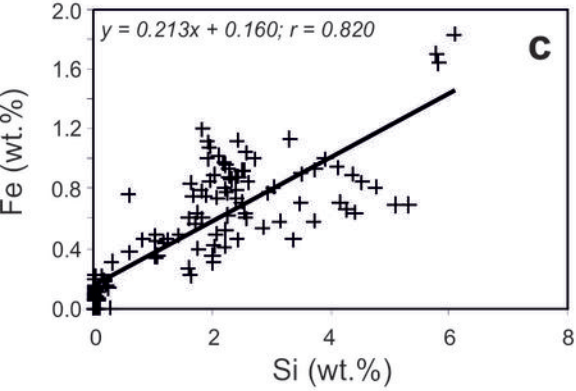
y = 0.213x + 0.160; r = 0.820
c
Fe (wt.%)
Si (wt.%)
2.0
1.6
1.2
0.8
0.4
0.0
0
2
4
6
8

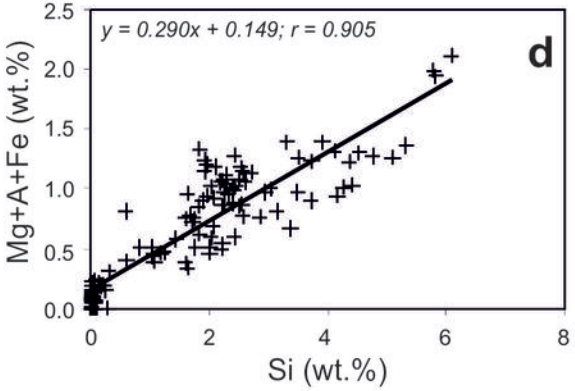
y = 0.290x + 0.149; r = 0.905
d
Mg+A+Fe (wt.%)
Si (wt.%)
2.5
2.0
1.5
1.0
0.5
0.0
0
2
4
6
8

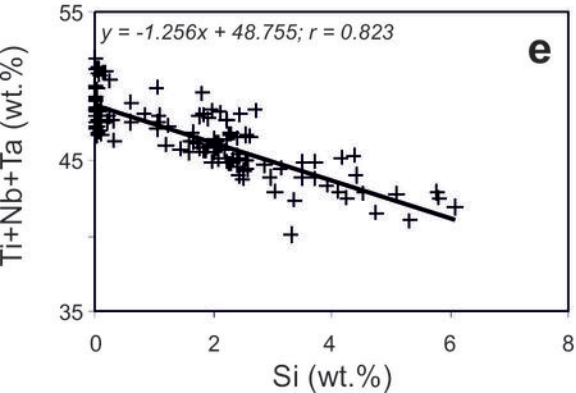
y = -1.256x + 48.755; r = 0.823
e
Ti+Nb+Ta (wt.%)
Si (wt.%)
55
45
35
0
2
4
6
8

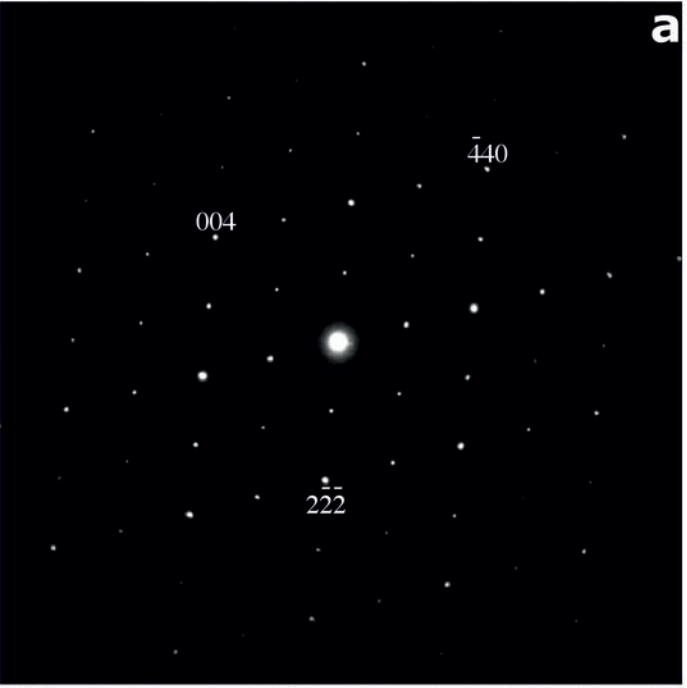
a
$\bar{4}40$
004
$\bar{2}\bar{2}2$

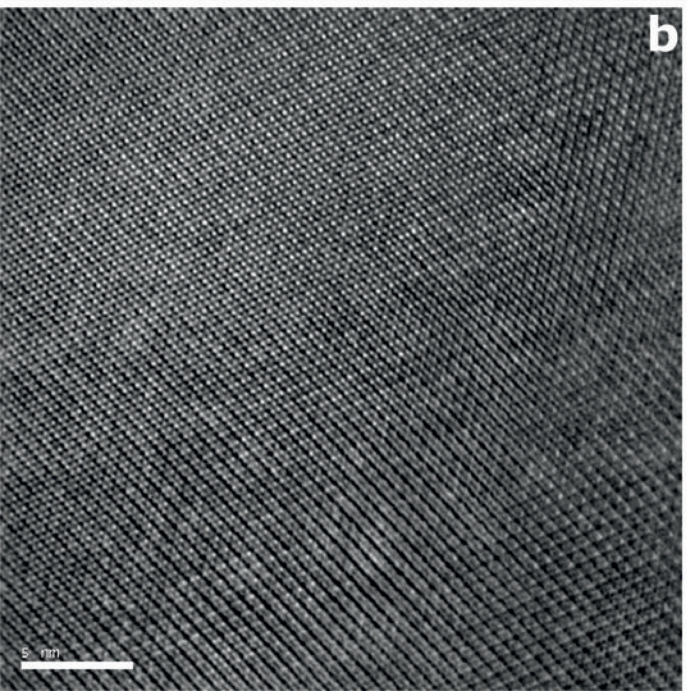
b
5 nm

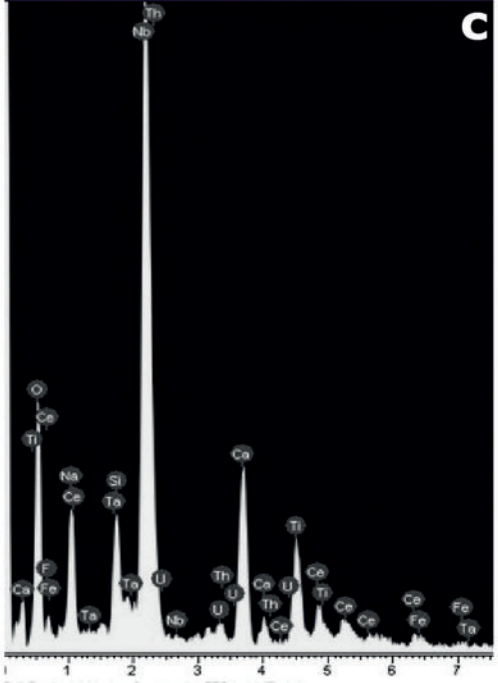
c
Th
Nb
O
Ce
Ti
Na
Ce
Si
Ta
Ca
Ti
F
Ce
Ca
Th
U
Ta
Th
U
U
Ca
U
Th
Ce
Ce
Ti
Ce
Ce
Ce
Fe
Fe
Ta
1
2
3
4
5
6
7

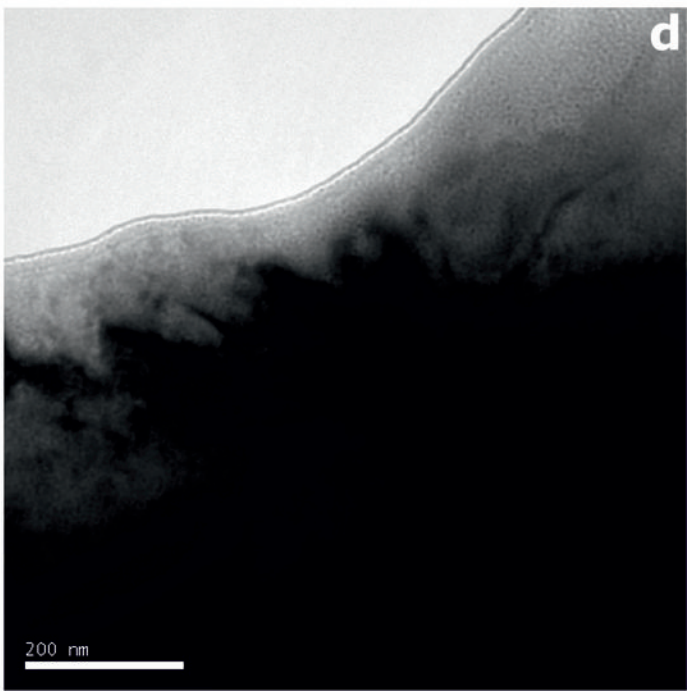
d
200 nm

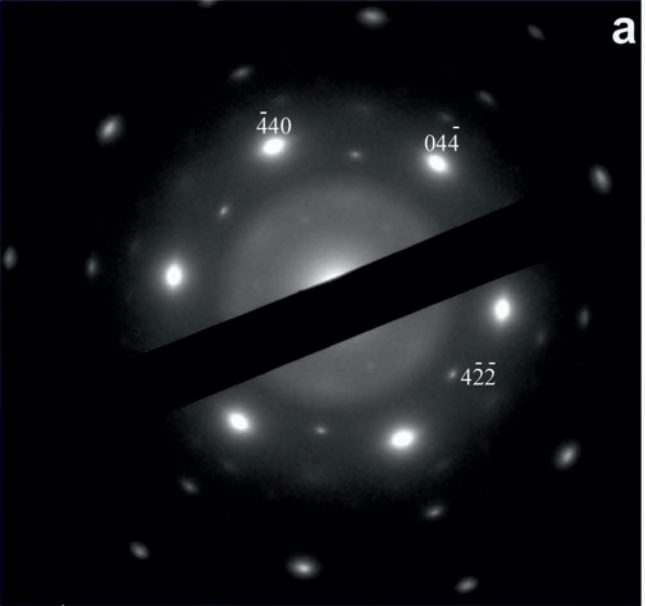
a
$\bar{4}40$
$044\bar{}$
$4\bar{2}\bar{2}$

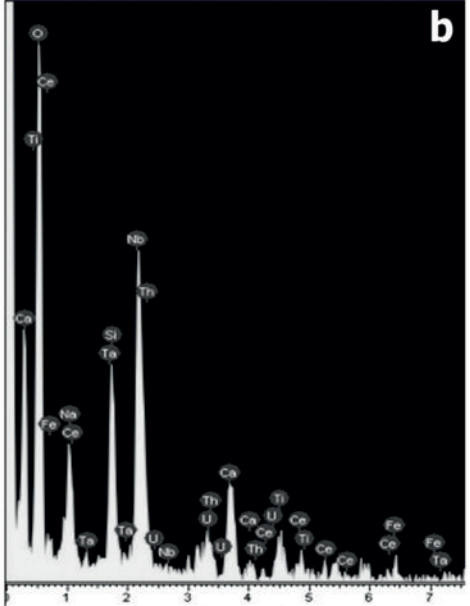
b
O
Ce
Ti
Ca
Nb
Th
Si
Ta
Na
Fe
Ce
Ta
Ta
U
Nb
Th
U
U
Ca
Ca
Ce
Ce
Th
Ti
U
Ce
Ti
Ce
Ce
Fe
Ce
Fe
Ta
1
2
3
4
5
6
7

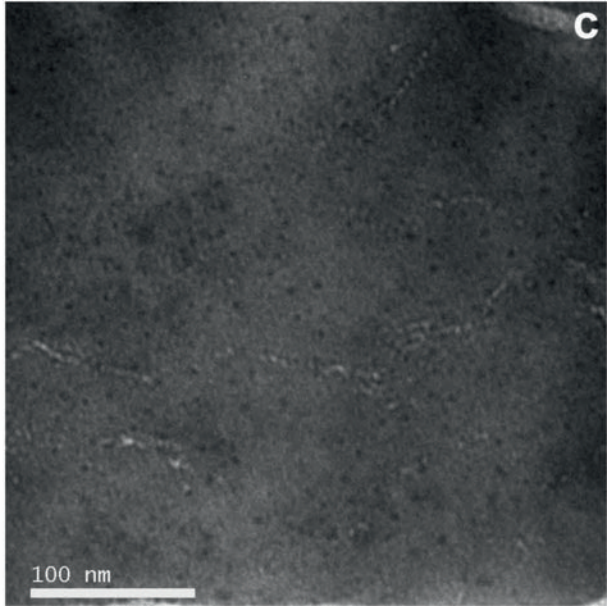
c
100 nm

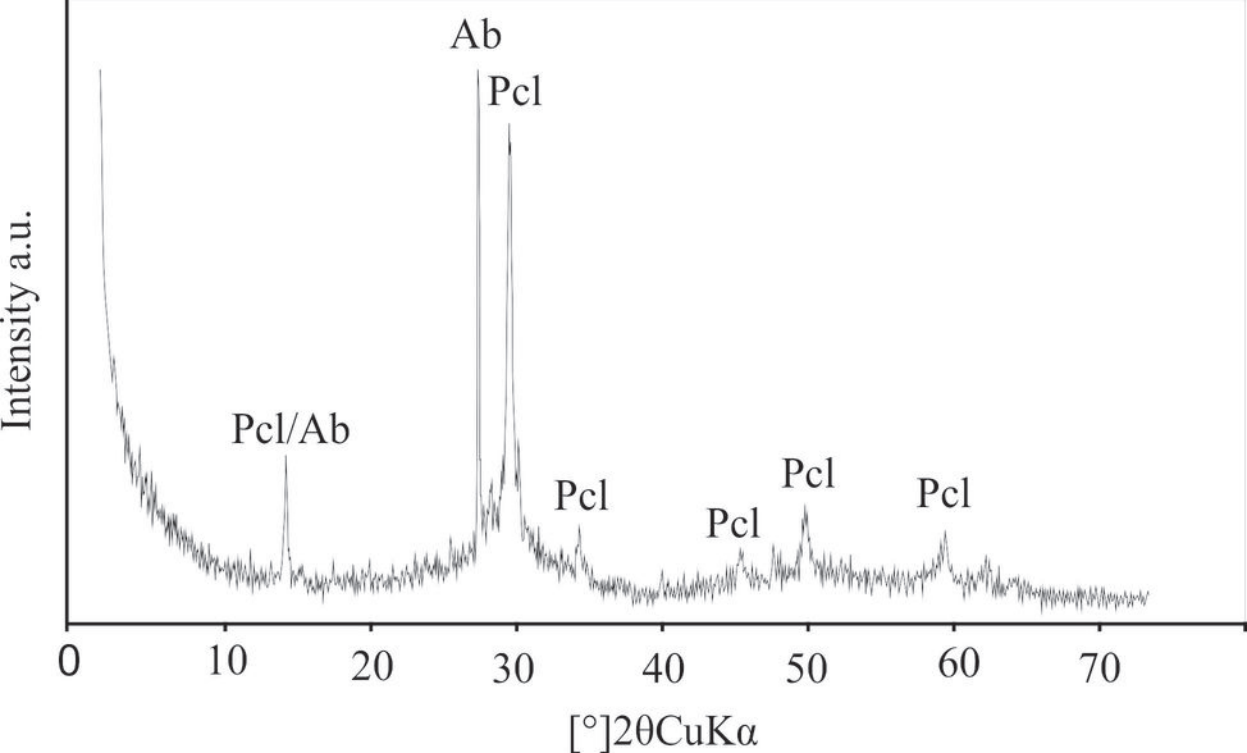
Ab
Pcl
Pcl/Ab
Pcl
Pcl
Pcl
Pcl
Intensity a.u.
0
10
20
30
40
50
60
70
[°]2θCuKα

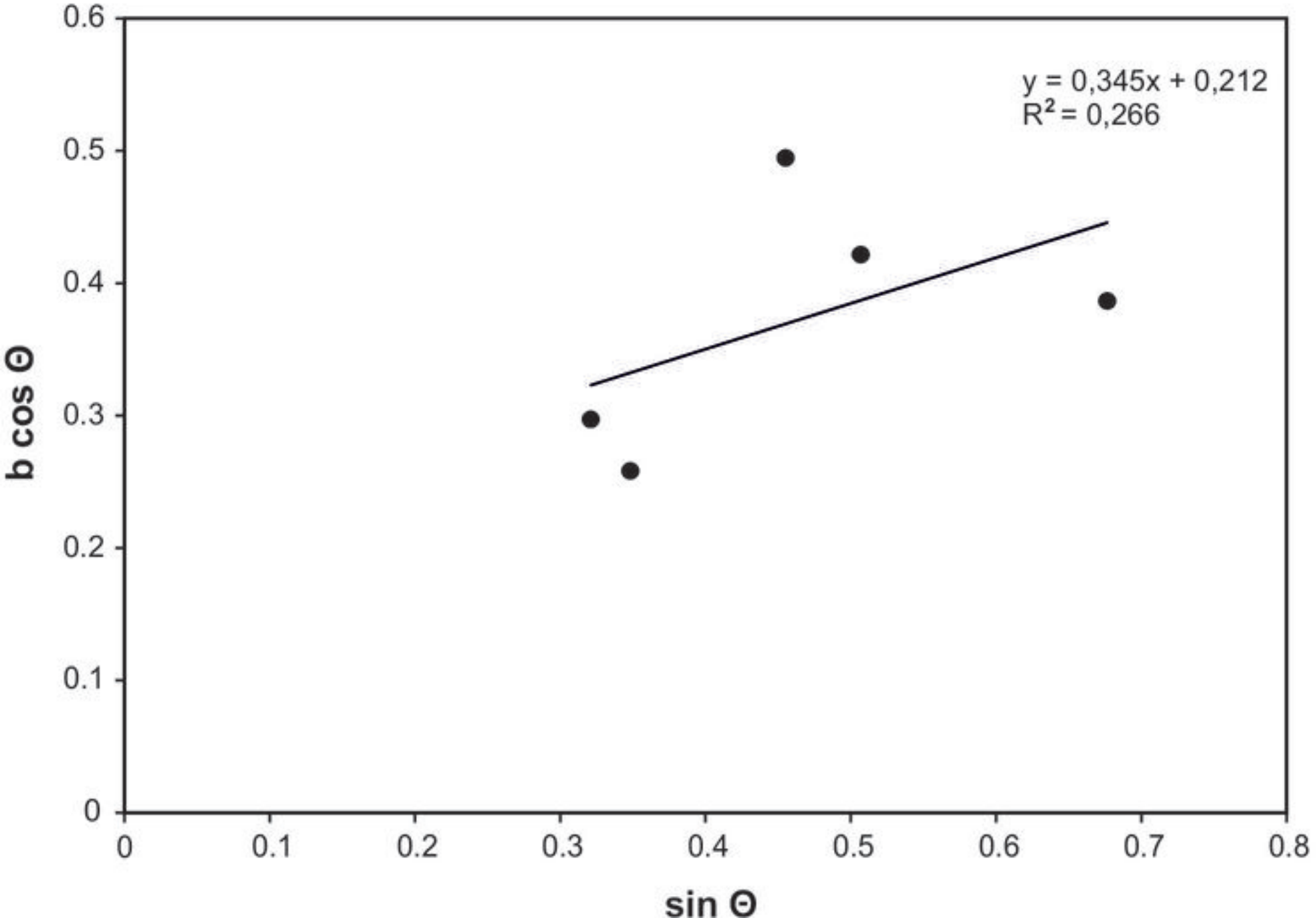
y = 0,345x + 0,212
R² = 0,266
b cos Θ
sin Θ
0
0.1
0.2
0.3
0.4
0.5
0.6
0.7
0.8

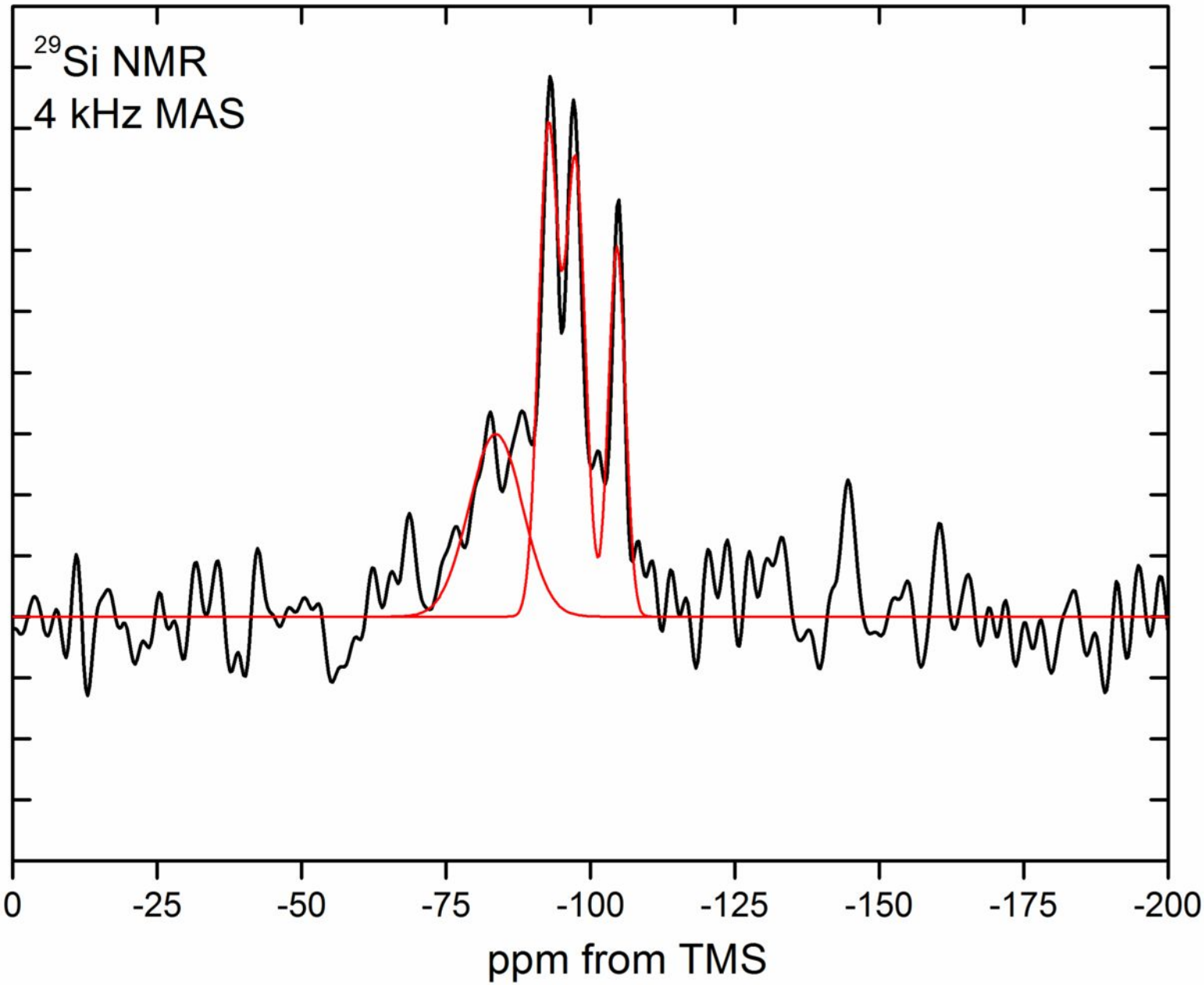
^{29}Si NMR
4 kHz MAS
0
-25
-50
-75
-100
-125
-150
-175
-200
ppm from TMS

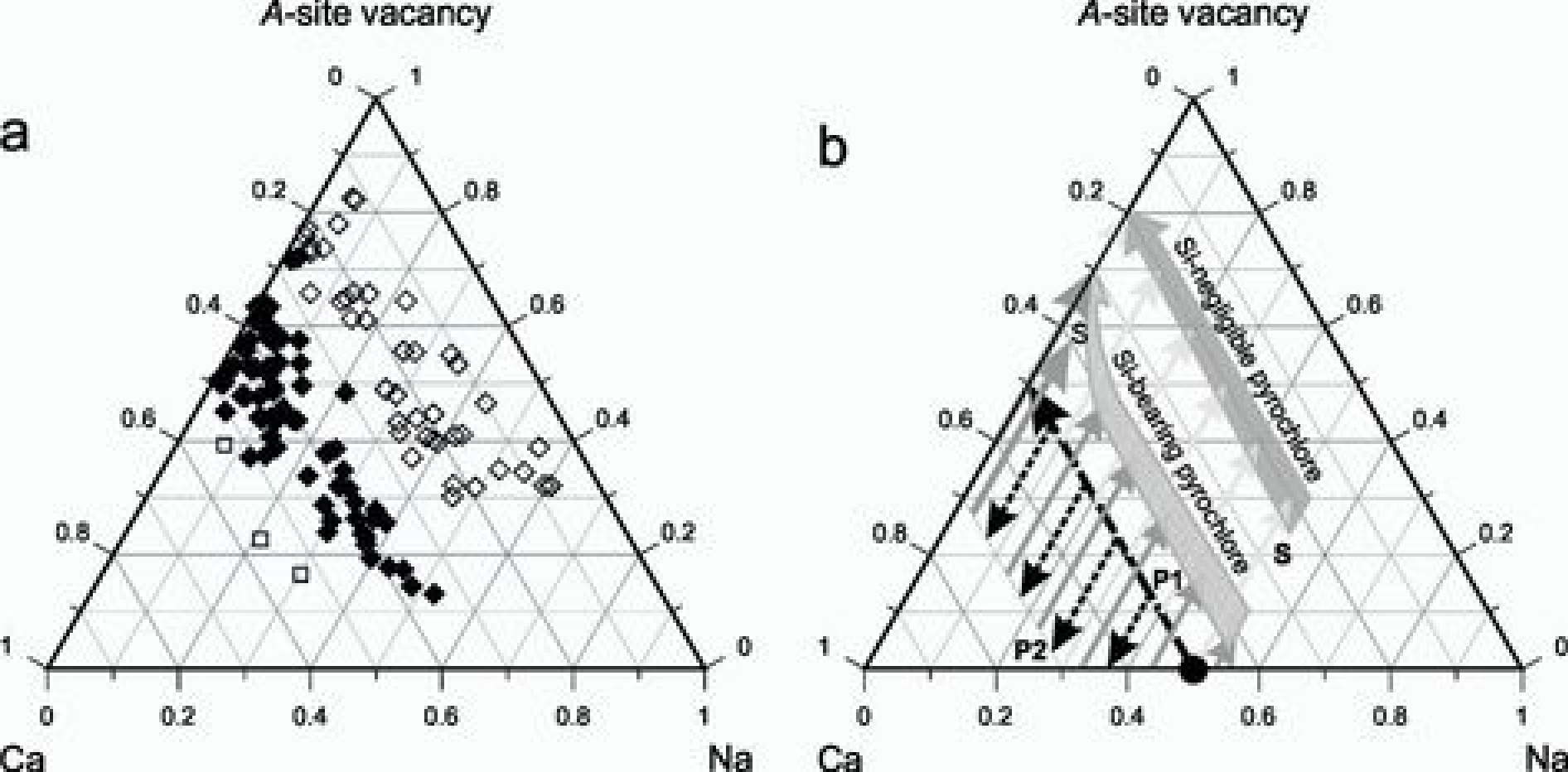
a
A-site vacancy
0
1
0.2
0.8
0.4
0.6
0.6
0.4
0.8
0.2
1
0
0
0.2
0.4
0.6
0.8
1
Ca
Na
b
A-site vacancy
Si-negligible pyrochlore
Si-bearing pyrochlore
S
P1
P2
Ca
Na

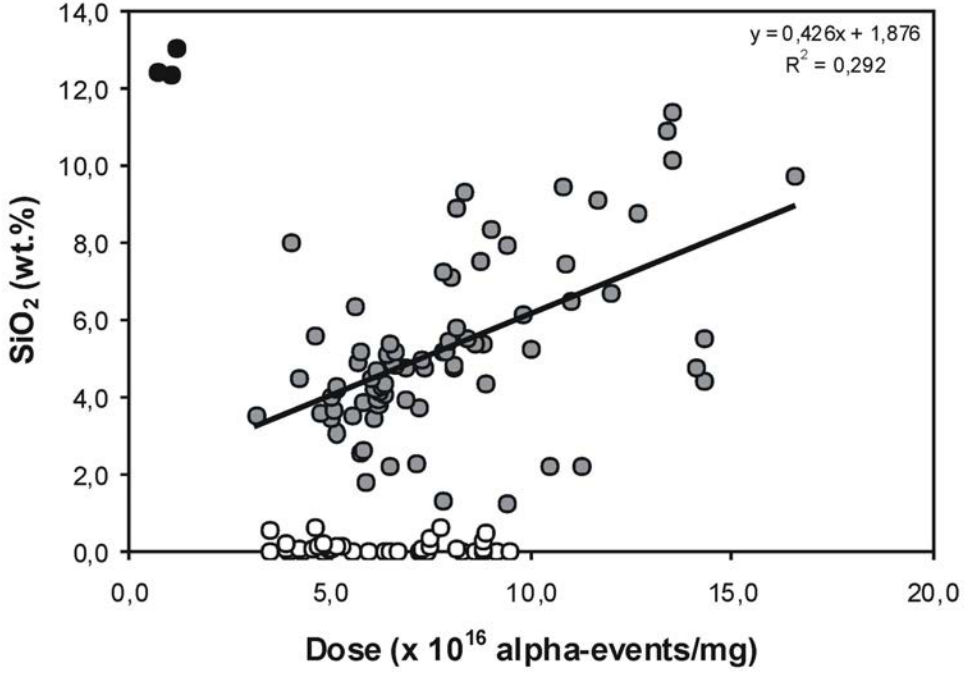
y = 0,426x + 1,876
R2 = 0,292
14,0
12,0
10,0
8,0
6,0
4,0
2,0
0,0
SiO2 (wt.%)
0,0
5,0
10,0
15,0
20,0
Dose (x 10^16 alpha-events/mg)